Bubbly flow structure in hydraulic jump

H. Chanson

Reader in Civil Engineering, The University of Queensland, Brisbane QLD 4072, Australia

Abstract

In an open channel, a hydraulic jump is the rapid transition from super- to sub-critical flow associated with strong turbulence and air bubble entrainment in the mixing layer. New experiments were performed at relatively large Reynolds numbers using phase-detection probes. Some new signal analysis provided characteristic air–water time and length scales of the vortical structures advecting the air bubbles in the developing shear flow. An analysis of the longitudinal air–water flow structure suggested little bubble clustering in the mixing layer, although an interparticle arrival time analysis showed some preferential bubble clustering for small bubbles with chord times below 3 ms. Correlation analyses yielded longitudinal air–water time scales $T_{xx} V_1 / d_1$ of about 0.8 in average. The transverse integral length scale Z/d_1 of the eddies advecting entrained bubbles was typically between 0.25 and 0.4, irrespective of the inflow conditions within the range of the investigations. Overall the findings highlighted the complicated nature of the air–water flow.

© 2006 Elsevier Masson SAS. All rights reserved.

Keywords: Hydraulic jumps; Bubbly flow structures; Integral time scales; Transverse length scales; Bubble chord time distributions; Interparticle arrival time; Clustering; Air bubble entrainment

1. Introduction

In an open channel, the rapid transition from a high-velocity flow into a slow flow is a hydraulic jump that is characterised by strong turbulent mixing and air bubble entrainment (Fig. 1). Basic studies of bubbly flow properties in hydraulic jumps included Rajaratnam [1] and Thandaveswara [2] (Table 1). A 'milestone' contribution was the work of Resch and Leutheusser [3] who showed first that the air entrainment, momentum transfer and energy dissipation processes are strongly affected by the inflow conditions. More recent studies are summarised in Table 1. Despite these, the bubbly flow structure and the relevant characteristic time and length scales are not well known.

It is the purpose of this paper to present new experimental results obtained with a hydraulic jump with partially-developed inflow. First, the experimental apparatus is described in details. Then basic air-water flow properties are presented. In the later parts, the streamwise structure of the bubbly flow and the characteristic time and length scale results are discussed.

E-mail address: h.chanson@uq.edu.au (H. Chanson).
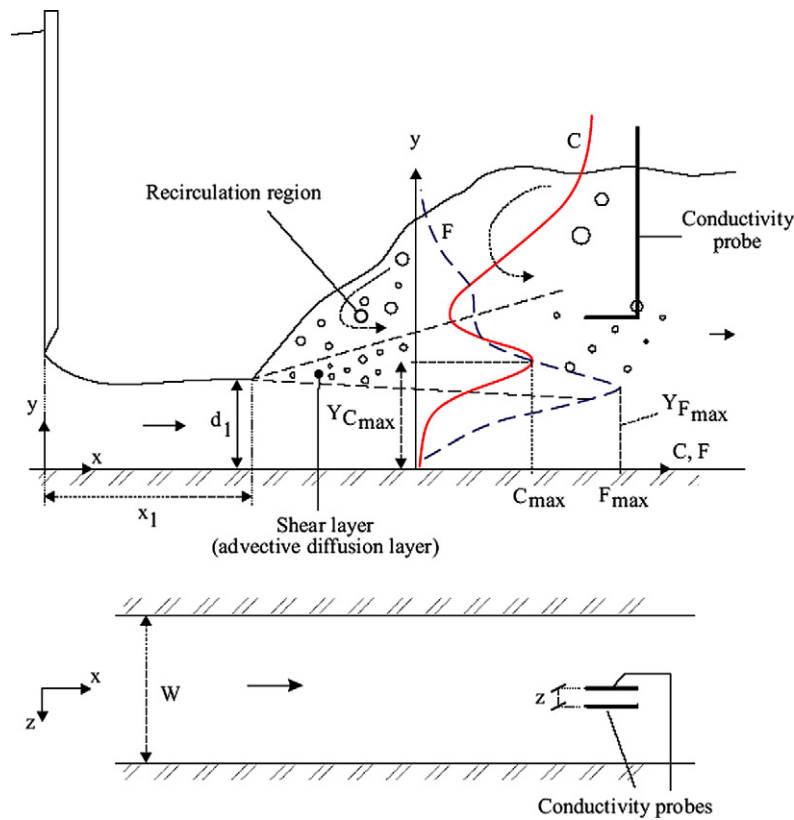*URL:* http://www.uq.edu.au/~e2hchans (H. Chanson).

Fig. 1. Sketch of air bubble entrainment in hydraulic jump.

2. Experimental apparatus

New experiments were performed in two horizontal channels at the University of Queensland. One flume was 3.2 m long, 0.25 m wide with glass bottom and sidewalls. The second channel was 3.2 long, 0.5 m wide with glass sidewalls and a PVC bed. Both channels were fed by a constant head tank.

The water depths were measured using rail mounted pointer gauges with an accuracy of 0.2 mm. The flow rates were measured with a 90° V-notch weir in the narrow flume and with a Venturi meter in the wide flume. Both systems were calibrated in-situ and the percentage of error was expected to be less than 2%.

Air–water flow properties were measured with two single-tip conductivity probes (inner electrode $\varnothing = 0.35$ mm). The reference probe was always located on the channel centreline ($z = 0$) while the second identical probe was separated in the transverse direction by a known spacing z (Figs. 1 and 2B). Both probe sensors were located at the same vertical and streamwise distances y and x respectively. The probes were excited by an electronic system (Ref. AS25240) designed with a response time of less than 10 µs. The signal outputs were scanned at 20 kHz per probe sensor for 45 s. The probe displacement in the vertical direction was controlled by a fine adjustment system (error < 0.1 mm).

Further details on the experimental apparatus as well as the full data sets were reported in Chanson [4].

2.1. Signal processing

The measurement principle of conductivity probes is based upon the difference in electrical resistivity between air and water. Typical probe signals are shown in Fig. 2 for the two probes placed at the same streamwise and vertical locations, but separated transversely by $z = 11.5$ mm. (In Fig. 2A, the air and water voltages are about $+0.3$ V and $+4.25$ V respectively.) The air–water flow properties were calculated using a single threshold technique and the threshold was set at about 45 to 55% of the air–water voltage range. A sensitivity analysis was conducted with thresh-

Table 1
Detailed experimental investigations of air entrainment in hydraulic jumps

Reference (1)	Flow conditions (2)	Measurement technique(s) (3)	Comments (4)
Rajaratnam [1]	$Fr_1 = 2.68$ to 8.72, $V_1 = 1.3$ to 4.35 m/s, $d_1 = 0.0254$ m	Conductivity probe	$W = 0.308$ m
Resch and Leutheusser [3]		Conical hot-film probe DISA 55A87 (0.6 mm sensor size)	$W = 0.39$ m
	$Fr_1 = 2.98$ & 8.04, $V_1 = 1.84$ & 2.78 m/s, $d_1 = 0.039$ & 0.012 m, $x_1 = 0.39$ & 0.122 m		P/D inflow conditions
	$Fr_1 = 3.26$ & 7.32, $V_1 = 2.5$ & 2.0 m/s, $d_1 = 0.039$ & 0.012 m, $x_1 = 2.44$ & 7.8 m		F/D inflow conditions
Thandaveswara [2]	$Fr_1 = 7.16$ to 13.31, $V_1 = 2.18$ to 4.60 m/s, $d_1 = 0.0107$ to 0.152 m $x_1 = 0.23$ m, P/D inflow conditions	Pitot tube (3.2 mm external $\varnothing$), Conductivity probe: double tip (4 mm tip spacing)	$W = 0.6096$ m
Babb and Aus [26]	$Fr_1 = 6.0$, $V_1 = 3.51$ m/s, $d_1 = 0.035$ m, P/D inflow conditions	Conical hot-film probe DISA 55R42 (0.4 mm sensor size)	$W = 0.46$ m
Chanson [5]	$Fr_1 = 5.0$ to 8.1, $V_1 = 1.97$ to 3.19 m/s, $d_1 = 0.016$ to 0.017 m, $x_1 = 0.7$ to 0.96 m, P/D inflow conditions ($\delta/d_1 = 0.45$ to 0.95 (m))	Pitot tube: 3.3 mm external $\varnothing$), Conductivity probe (single tip, 0.35 mm inner electrode)	$W = 0.25$ m
Mossa and Tolve [6]	$Fr_1 = 6.42$ to 7.3, $V_1 = 2.85$ to 3.12 m/s, $d_1 = 0.0185$ to 0.0202 m, $x_1 = 0.90$ m, P/D inflow conditions	Video-imaging (CCD, 5E+5 pixels, 16.8E+6 levels of grey pr pixel)	$W = 0.40$ m
Chanson and Brattberg [7]	$Fr_1 = 6.33$ & 8.48, $V_1 = 2.34$ & 3.14 m/s, $d_1 = 0.014$ m, $x_1 = 0.50$ m, P/D inflow conditions ($\delta/d_1 = 0.65$ (m))	Pitot tube: 3.3 mm external $\varnothing$), Conductivity probe (double tip, 0.025 mm inner electrode, 8 mm tip spacing)	$W = 0.25$
Murzyn et al. [8]	$Fr_1 = 2.0$ to 4.8, $V_1 = 1.50$ to 2.19 m/s, $d_1 = 0.021$ to 0.059 m, $x_1 = 0.28$ to 0.36 m, P/D inflow conditions ($\delta/d_1 = 0.18$ to 0.36 (c))	Optical fibre probe (double tip, 0.010 mm $\varnothing$, 1 mm tip spacing)	$W = 0.3$ m
Present study	$Fr_1 = 4.6$ to 8.6, $V_1 = 1.7$ to 4.0 m/s, $d_1 = 0.012$ to 0.029 m, $x_1 = 0.5$ & 1.0 m, P/D inflow conditions ($\delta/d_1 = 0.6$ to 0.7 (m))	Conductivity probes (single tip, 0.35 mm inner electrode)	P/D inflow conditions $W = 0.25$ and 0.5 m

Notes: F/D: fully-developed; P/D: Partially-developed; W: channel width; (c): calculated; (m) measured.

olds between 40 and 60% of the voltage range, showing little effect of the threshold on the air–water flow properties (e.g. error less than 1% on void fraction) as previously observed by Herringe and Davis [9] and Toombes [10].

The basic probe outputs were the void fraction C, the bubble count rate F defined as the number of bubbles impacting the probe tip per second, and the air chord time distribution where the chord time is defined as the time spent by the bubble on the probe tip. Statistical analyses of chord time distributions yielded median chord time, standard deviation, skewness and kurtosis. Interparticle arrival times were also calculated and analysed.

With two probes simultaneously sampled, the signals were analysed in terms of the auto-correlation and cross-correlation functions R_{xx} and R_{xz} respectively (Fig. 3). Basic results included the maximum cross-correlation coefficient $(R_{xz})_{\max}$, and the integral time scales T_{xx} and T_{xz} where:

$$T_{xx} = \int_{\tau=0}^{\tau=\tau(R_{xx}=0)} R_{xx}(\tau)\, d\tau, \tag{1}$$
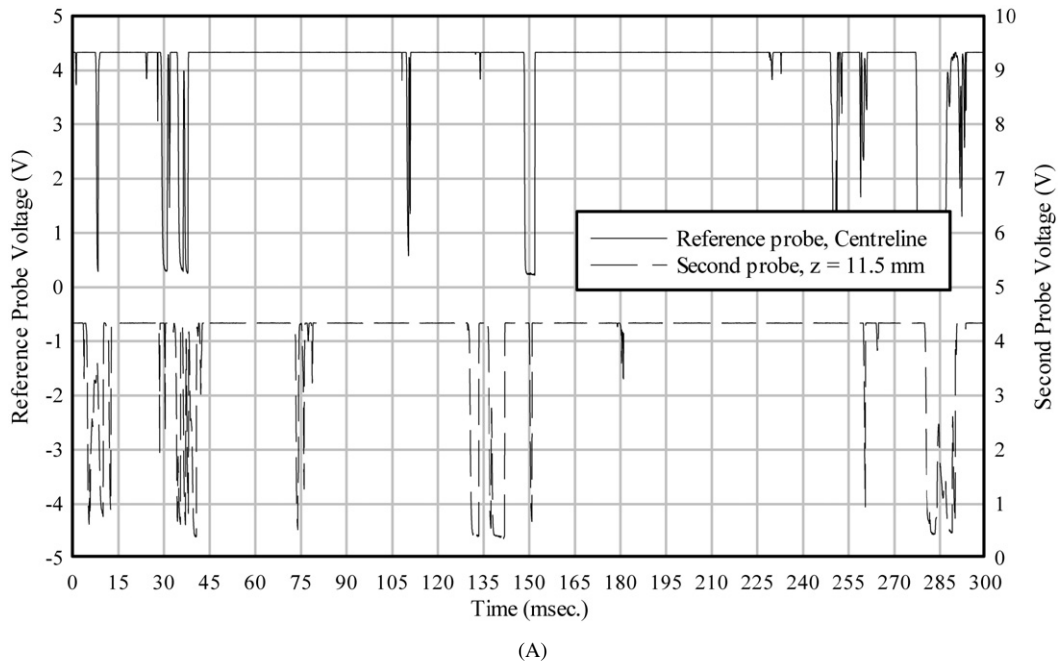
(A)

(B)

Fig. 2. Air–water flow measurements with two conductivity probes side-by-side. (A) Signal outputs in the shear layer of a hydraulic jump – transverse probe separation $z = 11.5$ mm, $C = 0.156$, $F = 136.7$ Hz, $y/d_1 = 0.91$, $Fr_1 = 8.6$, $d_1 = 0.024$ m, $x_1 = 1.0$ m, $x - x_1 = 0.2$ m, $W = 0.5$ m. (B) Two probes separated by $z = 10.5$ mm, flow direction from bottom left to top right – local air–water flow properties: $C = 0.79$, $F = 20.6$ Hz, $y/d_1 = 4.15$, $Fr_1 = 7.9$, $d_1 = 0.024$ m, $x_1 = 1$ m, $x - x_1 = 0.2$ m, $W = 0.25$ m.

$$T_{xz} = \int\limits_{\tau = \tau(R_{xz} = (R_{xz})_{max})}^{\tau = \tau(R_{xz} = 0)} R_{xz}(\tau)\, d\tau \tag{2}$$

with R_{xx} being the normalised auto-correlation function of the reference probe output signal, τ the time lag, and R_{xz} the normalised cross-correlation function between the two probe output signals (Fig. 3A). Fig. 3B illustrates some
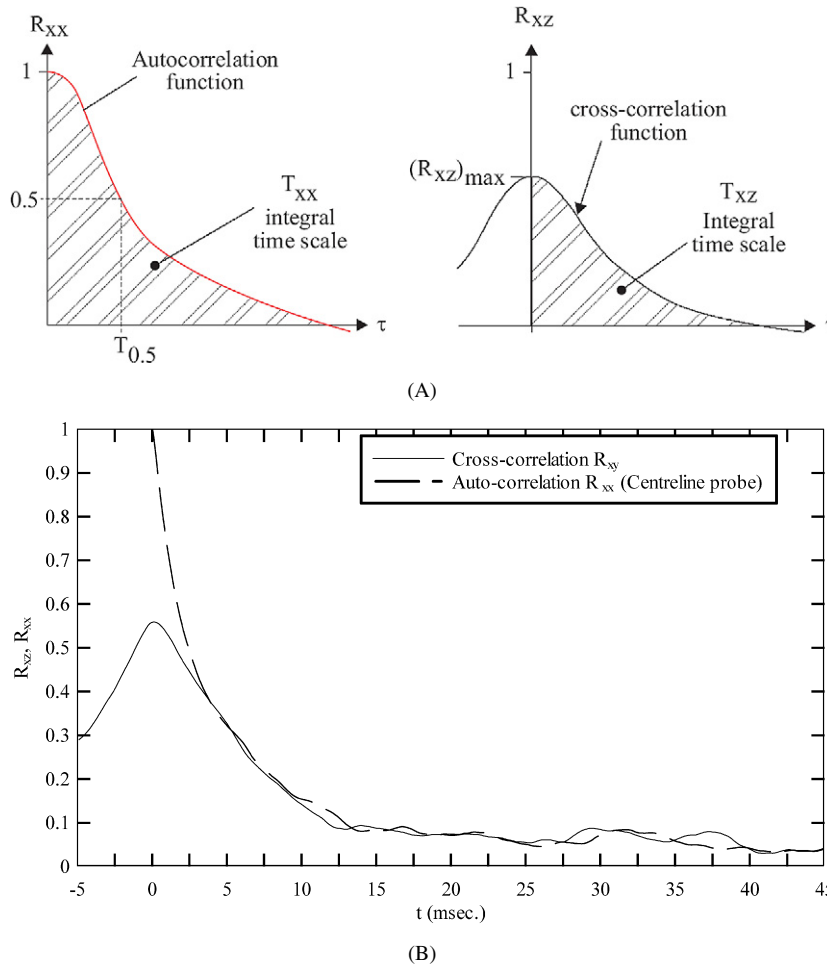
Fig. 3. Auto- and cross-correlation functions for two identical single-tip conductivity probes separated by a transverse distance z. (A) Definition sketch. (B) Experimental data: $z = 2.9$ mm, $C = 0.37$, $F = 156$ Hz, $y/d_1 = 1.47$, $Fr_1 = 7.9$, $d_1 = 0.0245$ m, $x_1 = 1.0$ m, $x - x_1 = 0.1$ m, $W = 0.25$ m.

typical auto- and cross-correlation data. When some identical experiments were repeated with different transverse spacings z, a characteristic length scale was calculated as:

$$Z = \int\limits_{z=0}^{z=z((R_{xy})_{max}=0)} (R_{xz})_{max}\, dz \tag{3}$$

where the transverse length scale Z is a function of the inflow conditions and streamwise position $(x - x_1)$. The length scale Z represented a transverse length scale of vortical structures in the hydraulic jump.

2.2. Experimental flow conditions

Clear water velocity measurements were performed in the supercritical inflows. The data showed that the inflow conditions were partially-developed for all investigated flow conditions. Herein the air–water flow properties were studied specifically in the developing air–water flow region: i.e., $(x - x_1)/d_1 \leqslant 20$ where x is the longitudinal distance from the sluice gate, x_1 is the distance from the gate to the jump toe and d_1 is the upstream flow depth which was measured typically 10 to 20 cm upstream of the jump toe.

Preliminary experiments were performed in both channels with inflow conditions within $0.012 \leqslant d_1 \leqslant 0.027$ m, $4.6 \leqslant Fr_1 \leqslant 8.6$ and $1.8\text{E}+4 \leqslant Re_1 \leqslant 1\text{E}+5$ where $Fr_1 = V_1/\sqrt{gd_1}$ is the inflow Froude number, $Re_1 = \rho_w V_1 d_1/\mu_w$

Table 2
Summary of detailed experimental investigations

Run	Q_w (m³/s)	d_1 (m)	V_1 (m/s)	W (m)	x_1 (m)	Fr_1	Re_1	W/d_1	Remarks
(1)	(2)	(3)	(4)	(5)	(6)	(7)	(8)	(9)	(9)
051117	0.0096	0.029	2.67	0.25	1.0	5.01	7.7E+4	19	
051123-25	0.0237	0.0245	3.60	0.25	1.0	7.9	9.5E+4	10	$z = 2.9, 10.5, 17$ mm
051202	0.0344	0.0265	2.60	0.5	1.0	5.1	6.8E+4	19	$z = 11.5$ mm
051206	0.0494	0.0238	4.14	0.5	1.0	8.6	9.8E+4	21	$z = 11.5$ mm

Note: Q_w: water discharge.

is the inflow Reynolds number, V_1 is the inflow velocity, g is the gravity acceleration, and ρ_w and μ_w are the water density and dynamic viscosity respectively. The results were reported in Chanson [4]. They showed that the air–water flow properties obtained at low Reynolds numbers could not be scaled up based upon a Froude similitude. That is, some scale effects in terms of void fraction and bubble count rate distributions were experienced for $d_1 \leqslant 0.014$ m and $Re_1 \leqslant 4E+4$. Therefore the present study was focused on the high Reynolds number flow conditions (Table 2). Further, the experiments showed that the channel width ($0.25 \leqslant W \leqslant 0.5$ m) had no effect on the air–water flow properties for $Re_1 > 4E+4$.

3. Basic air–water flow properties

In a hydraulic jump, air entrainment occurs in the form of air bubbles and air packets entrapped at the impingement of the upstream jet flow with the roller. The air packets are broken up in very small air bubbles as they are entrained in the shear region which is characterised by large air contents and maximum bubble count rates. Once the entrained bubbles are advected into regions of lesser shear, bubble collisions and coalescence lead to larger air entities (bubbles, pockets) that are driven towards the free-surface by a combination of buoyancy and turbulent advection.

With partially-developed inflow, a key feature of the jump flow is the presence of an advective diffusion region in which the void fractions distributions exhibit a peak in the turbulent shear region as sketched in Fig. 1. This advective diffusion air layer was documented experimentally in past and present studies [4,6,7]. An example is shown in Fig. 4. With increasing distance ($x - x_1$) from the impingement, the peak void fraction C_{max} decreased while the diffusion layer broadened as seen in Fig. 4A. Experimental results indicated further the existence of a peak F_{max} in bubble count rate (Fig. 4B), but its location did not coincide with the locus of maximum void fraction as noticed by [7] and [8], and observed in the present study (Figs. 4A and 4B).

In the advective diffusion layer, the void fraction distributions followed closely an analytical solution of the diffusion equation for air bubbles:

$$C = \frac{Q_{air}/Q_w}{\sqrt{4\pi D^\# (x - x_1)/d_1}} \left(\exp\left(-\frac{1}{4D^\#} \frac{(y/d_1 - 1)^2}{(x - x_1)/d_1} \right) \right) + \exp\left(-\frac{1}{4D^\#} \frac{(y/d_1 + 1)^2}{(x - x_1)/d_1} \right) \right) \tag{4}$$

where Q_{air} is the volume air flow rate, Q_w is the water discharge, $D^\#$ is a dimensionless diffusivity: $D^\# = D_t/(V_1 d_1)$, D_t is the turbulent diffusivity which averages the effects of turbulent diffusion and of longitudinal velocity gradient, and x and y are the longitudinal and vertical distances measured from the channel intake and bed respectively. Eq. (4) was developed for both two-dimensional supported plunging jet and hydraulic jump flows [11,12], but it does not account for buoyancy effects in a horizontal channel. In practice, experimental data showed that the void fraction profiles are best predicted by an approximate form of Eq. (4):

$$C = \frac{Q_{air}/Q_w}{\sqrt{4\pi D^\# (x - x_1)/d_1}} \left(\exp\left(-\frac{1}{4D^\#} \frac{(y/d_1 - Y_{C_{max}}/d_1)^2}{(x - x_1)/d_1} \right) + \exp\left(-\frac{1}{4D^\#} \frac{(y/d_1 - Y_{C_{max}}/d_1)^2}{(x - x_1)/d_1} \right) \right) \tag{5}$$

where $y = Y_{C_{max}}$ is the vertical elevation where the void fraction is maximum $C = C_{max}$ (Fig. 1). Eq. (5) is compared with experimental data in Fig. 4A. Note that the dimensionless diffusivity $D^\#$ was deduced from the best data fit.
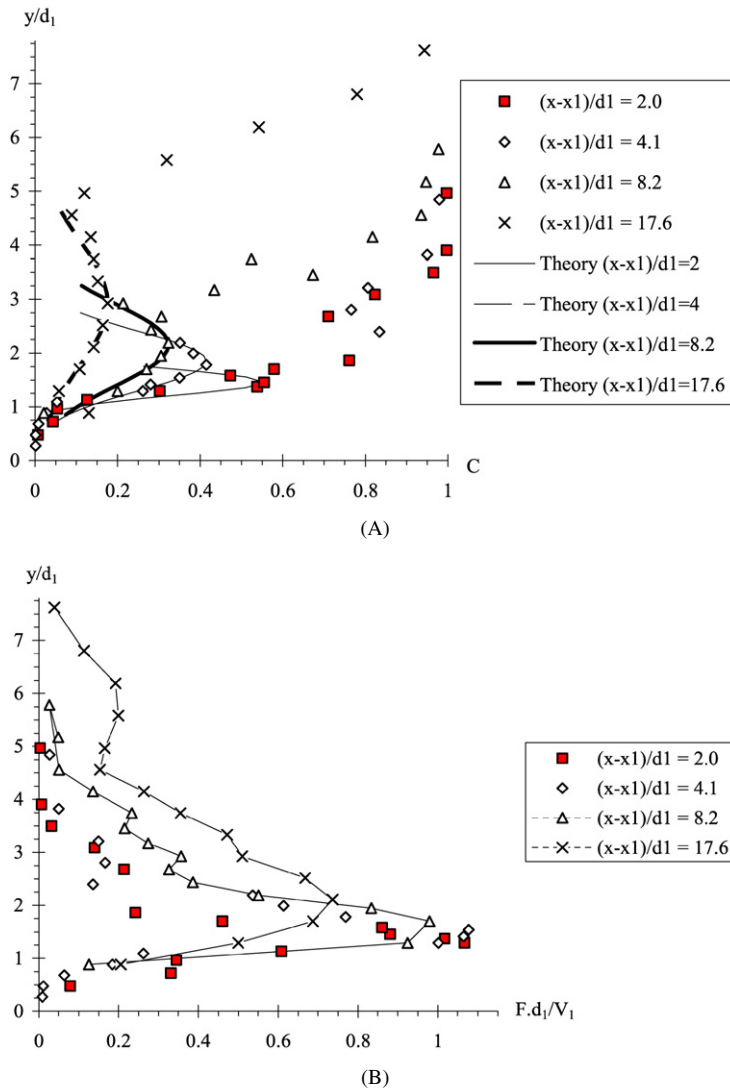
Fig. 4. Dimensionless distributions of void fraction and bubble count rate in a hydraulic jump with partially-developed inflow – $Fr_1 = 7.9$, $Re_1 = 9.5E+4$, $d_1 = 0.0245$ m, $x_1 = 1.0$ m, $W = 0.250$ m. (A) Dimensionless distributions of void fraction C – comparison with Eq. (5). (B) Dimensionless distributions of bubble count rate $F d_1 / V_1$.

Remark. The void fraction profiles showed some marked difference with some upper and lower regions of the flow. In the upper flow region, Murzyn et al. [8] suggested that the void fraction distributions followed a Gaussian error function:

$$C = \frac{1}{2}\left(1 + \mathrm{erf}\left(\frac{1}{2}\sqrt{\frac{V_1 d_1}{D'_\mathrm{t}}}\frac{(y - Y_{50})/d_1}{\sqrt{(x - x_1)/d_1}}\right)\right) \quad \text{upper free-surface} \tag{6}$$

where Y_{50} is the characteristic depth (m) where the void fraction is 50%, D'_t is the turbulent diffusivity of the upper interface and the function erf is:

$$\mathrm{erf}(u) = \frac{2}{\sqrt{\pi}} \int_0^u \exp(-t^2)\, \mathrm{d}t. \tag{7}$$

Eq. (6) was derived by Chanson [13] as an analytical solution of the advection/diffusion equation for air bubbles in water jets discharging into air with an uniform velocity distribution, for a diffusivity D'_t that is assumed independent

of the transverse direction y and which averages the effect of turbulence and longitudinal velocity gradient [11,14]. Eq. (6) is not applicable to a hydraulic jump roller "free-surface" although it fits the data [8,4].

4. Bubble chord time distributions

In a complicated flow such as a hydraulic jump, flow reversal and recirculation exist and phase-detection intrusive probe cannot discriminate accurately the direction nor magnitude of the velocity. Hence only chord time data are presented herein for the sake of accuracy. Fig. 5 shows typical normalised distributions of bubble chord time in the hydraulic jump. For each graph, the legend provides the location $(x - x_1, y/d_1)$, local air–water flow properties (C, F), and number of recorded bubbles N_{ab}. The histogram columns represent each the probability of bubble chord time in a 0.5 ms chord time interval. For example, the probability of air chord time from 1 to 1.5 ms is represented by the column labelled 1 ms. Bubble chord times larger than 15 ms are regrouped in the last column (>15). Fig. 6 presents typical vertical distributions of median chord time, standard deviation, skewness and excess kurtosis at several longitudinal locations for one inflow Froude number. Note that the bubble chord time is proportional to the bubble chord length and inversely proportional to the velocity. For a 1 m/s particle velocity, a 1 ms chord time would correspond to a 1 mm particle chord length.

First the data showed a broad spectrum of bubble chord times at each location. The range of air chord time extended over several orders of magnitude, including at low void fractions, from less than 0.1 ms to more than 15 ms. Second the distributions were skewed with a preponderance of small bubble chord times relative to the mean. The probability
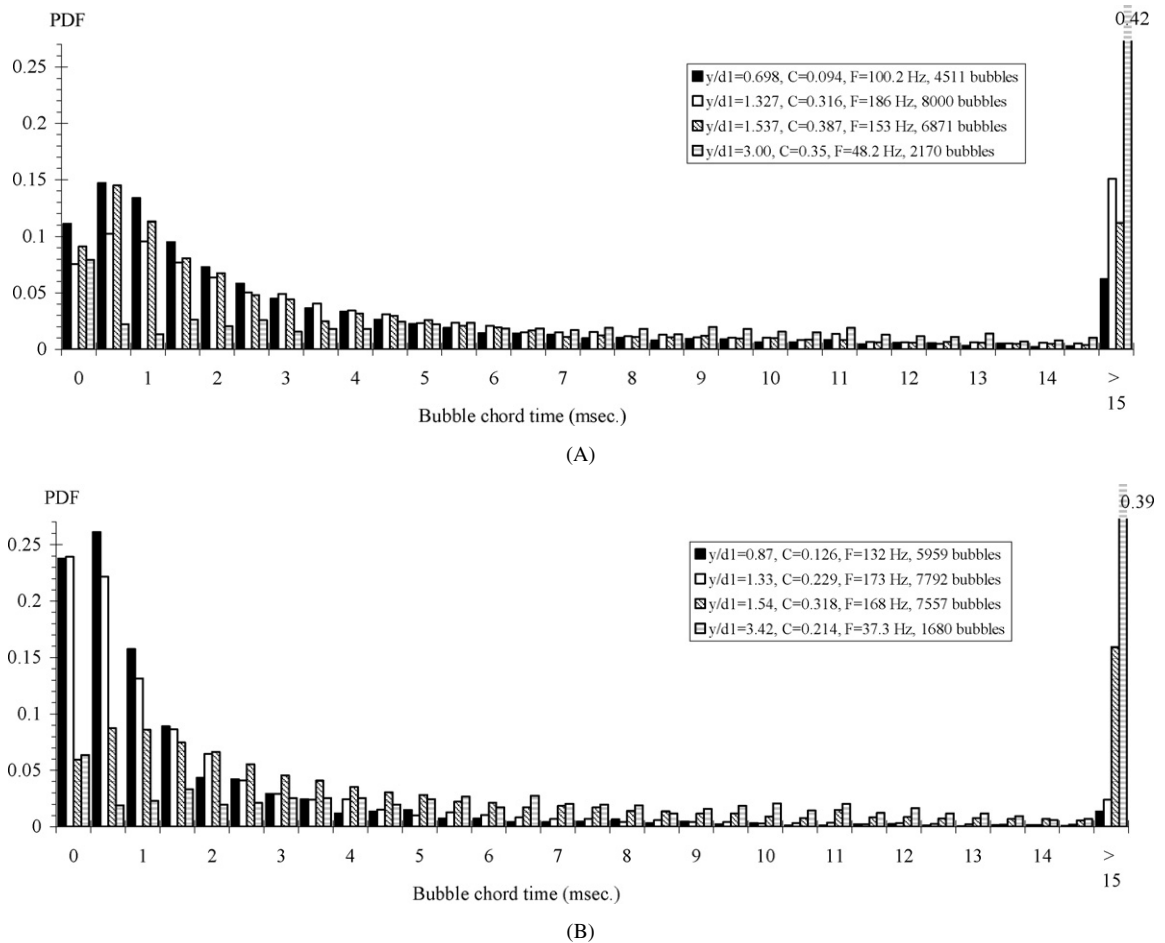

Fig. 5. Bubble chord time probability distributions in a hydraulic jump − $Fr_1 = 8.6$, $Re_1 = 9.8\text{E}+4$, $d_1 = 0.024$ m, $x_1 = 1.0$ m, $W = 0.50$ m, 0.5 ms chord time intervals. (A) $(x - x_1)/d_1 = 8.4$. (B) $(x - x_1)/d_1 = 12.6$.
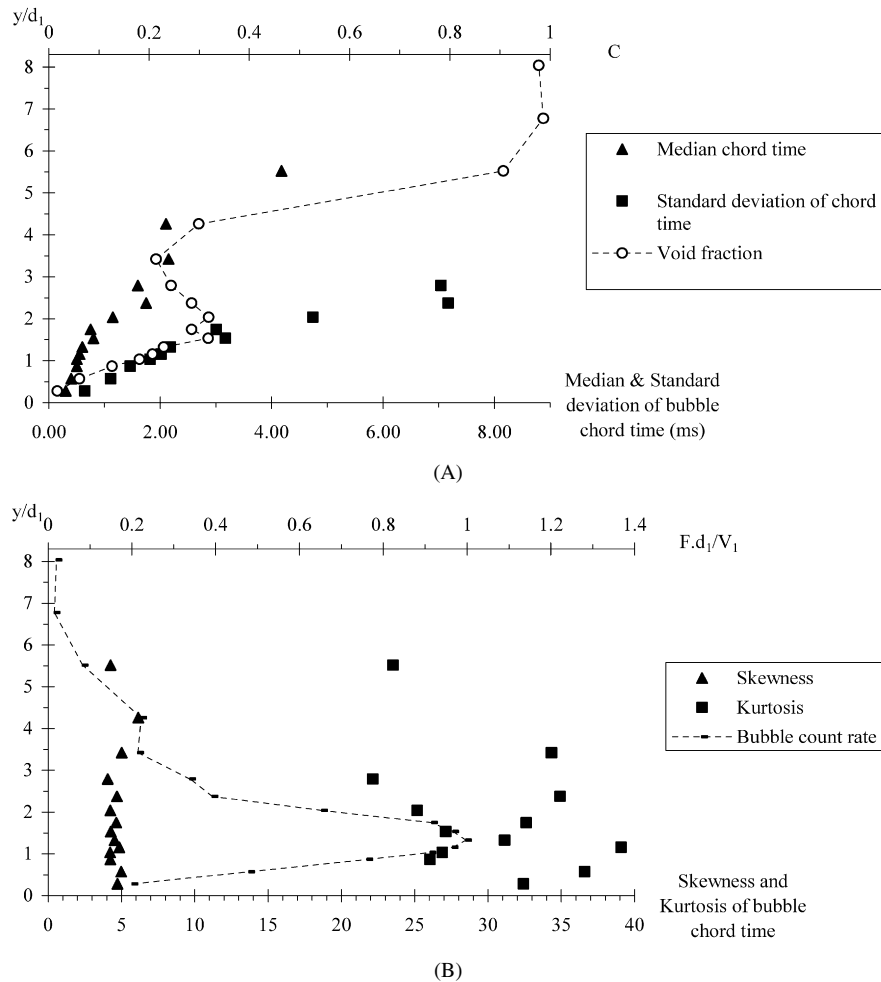
Fig. 6. Vertical distributions of median value, standard deviation, skewness and excess kurtosis of bubble chord times in a hydraulic jump – $Fr_1 = 8.5$, $Re_1 = 9.8\text{E}+4$, $d_1 = 0.024$ m, $x_1 = 1.0$ m, $W = 0.50$ m, $(x - x_1)/d_1 = 12.6$. (A) Distributions of median chord times and standard deviations – comparison with the distribution of void fraction. (B) Distributions of skewness and excess kurtosis – comparison with the distribution of bubble count rate.

distribution functions of bubble chord time tended to follow in average a log-normal distribution. A similar finding was observed in plunging jet flows (e.g. Chanson et al. [15]). Third, the bubble chord time distributions had a similar shape at most vertical locations y/d_1 although the air–water structures may differ substantially between the mixing and recirculation regions.

Vertical distributions of median chord time showed similar shapes at all cross-sections (e.g. Fig. 6A). At a given streamwise position $(x - x_1)$, a marked increase in bubble chord time was observed in the developing shear layer $(1 < y/d_1 < 3$ in Fig. 6). It was expected to reflect the presence of large air packets entrapped at the jump toe and advected in the mixing layer. The shape of vertical distributions of median chord times was close to some vertical distributions of Sauter diameter presented by Murzyn et al. [8]. In that study, bubble chord times were transformed into bubble diameter using the time-average velocity measured with a dual-tip optical fibre probe (1 mm between tips). Fig. 6 presents also typical vertical distributions of bubble chord time standard deviation, skewness and kurtosis. The results highlighted large standard deviations of chord time with ratios of standard deviations to median values larger than 2 to 5 typically. Large positive values of skewness and excess kurtosis were also observed (Fig. 6B). The findings reflected the broad range and skewed shape of the chord time probability distribution functions as well their peakiness (e.g. Fig. 5).

5. Clustering and particle grouping

In addition the signal outputs provide some information on the streamwise structure of the air–water flow including bubble clustering. A study of clustering events may be useful to infer if the formation frequency responds to some particular frequencies of the flow (e.g. [16,17]). However a concentration of bubbles within some relatively short intervals of time may indicate some clustering or it may be the consequence of a random occurrence. Fig. 7A shows a typical time series of bubble chord time measurements at one sampling location where the maximum bubble count rate occurred ($F = F_{max}$). Fig. 7B shows the occurrence of pairing in time at the same location. The binary pairing indicator is unity if the water chord time between adjacent bubbles is less than 10% of the median water chord time and zero otherwise. The grouping of vertical lines seen in Fig. 7B is an indication of patterns in which bubbles tend to form bubble "platoons".

One approach may be based upon the analysis of the water chord between two adjacent bubbles. If two bubbles are closer than a particular length or time scale, they can be considered a group of bubbles. The characteristic length/time scale may be related to the water chord statistics or to the bubble size itself, since bubbles within some distance may be influenced by the leading particle [17,18,27]). A typical result is presented in Fig. 8 where the criterion for cluster existence was a water chord time being less than 10% of the median. Fig. 8A shows the vertical distribution of the number of clusters per seconds (upper horizontal axis), and Fig. 8B presents the vertical distributions of the percentage of bubbles in clusters (lower horizontal axis) and average number of bubbles per cluster (upper horizontal axis) in the
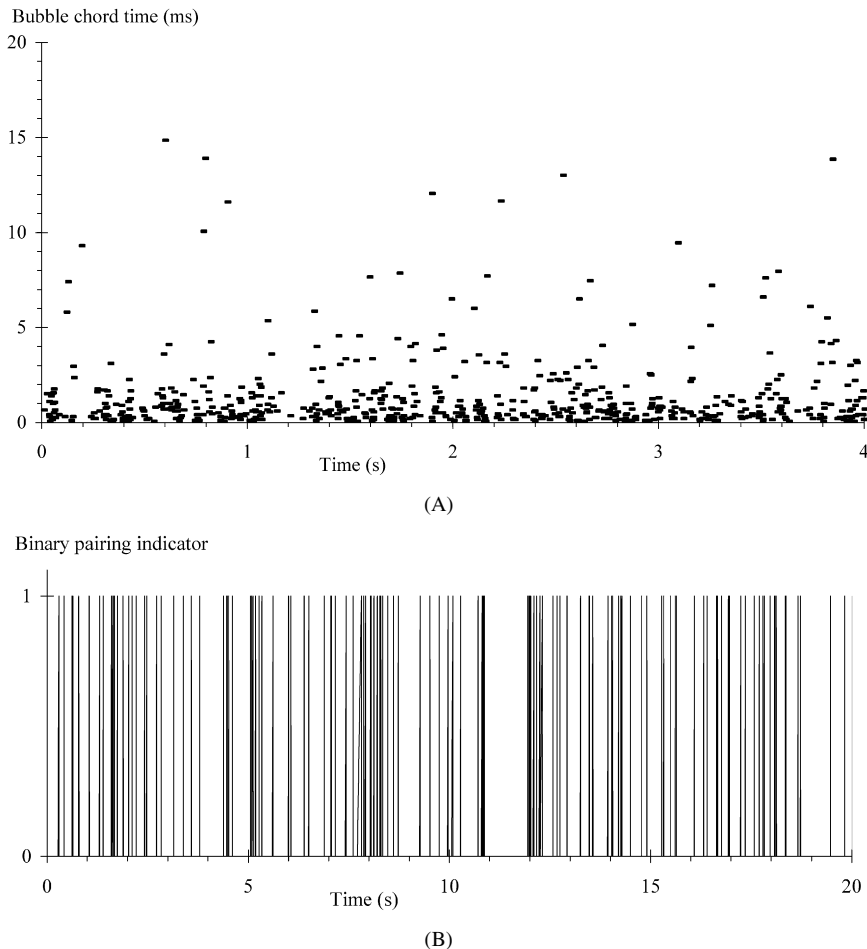

(A)

(B)

Fig. 7. Air–water flow structures in the developing shear layer of hydraulic jump – $Fr_1 = 8.5$, $Re_1 = 9.8E+4$, $d_1 = 0.024$ m, $x_1/d_1 = 40$, $W = 0.50$ m, $(x - x_1) = 0.40$ m, $y/d_1 = 1.33$, $C = 0.20$, $F = F_{max} = 158$ Hz. (A) Time records of entrained bubbles. (B) Binary pairing indicator of closely spaced bubble pairs in the developing shear layer (1 = water chord time less than 10% of median; 0 = otherwise).
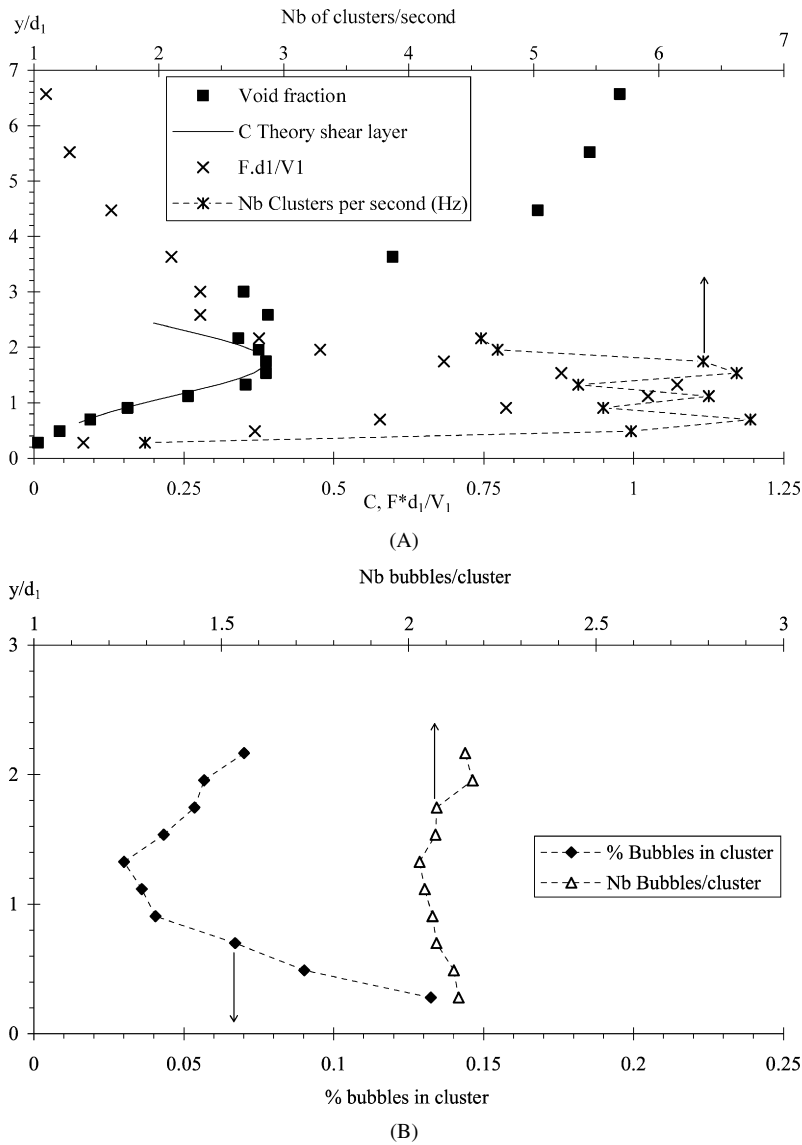
Fig. 8. Dimensionless distributions of percentage of bubbles in clusters, average number of bubbles per cluster and number of clusters per seconds – $Fr_1 = 8.5$, $Re_1 = 9.8E+4$, $d_1 = 0.024$ m, $x_1/d_1 = 40$, $(x − x_1)/d_1 = 12$, $W/d_1 = 20$ – cluster criterion: water chord time $< 10\%$ median water chord time. (A) Dimensionless distributions of percentage of bubbles in clusters, void fraction and average number of clusters per seconds. (B) Dimensionless distributions of percentage of bubbles in clusters and average number of bubbles per cluster.

advective diffusion region. In Fig. 8A, note the behaviour (i.e., oscillations) of the number clusters per second data for $0.5 < y/d_1 < 2$. The matter ought to be further investigated, possibly with a longer scan duration. Overall the results (e.g. Fig. 8) showed in average a relatively small percentage (5 to 10%) of bubbles that were part of cluster structures. It is likely that this derived from some unique features of air–water flow structures in hydraulic jumps.

For a dispersed phase, a complementary approach is based upon the analysis of interparticle arrival times [19, 20,16,17]. "Random" dispersed flows are those whose interparticle arrival time distributions follow inhomogeneous Poisson statistics. That is, the interparticle time distribution function in steady-random dispersed flows is:

$$f(t) = \frac{\lambda(T_{\text{scan}} - t)\exp(-\lambda t)}{\lambda T_{\text{scan}} - 1 + \exp(-\lambda T_{\text{scan}})} \tag{8}$$

where t is the interparticle arrival time, T_{scan} is the sampling duration (herein 45 s), $\lambda = N_{ab}/T_{\text{scan}}$ and N_{ab} is the number of particles [21]. Eq. (8) would describe an ideal dispersed flow driven by a superposition of Poisson processes
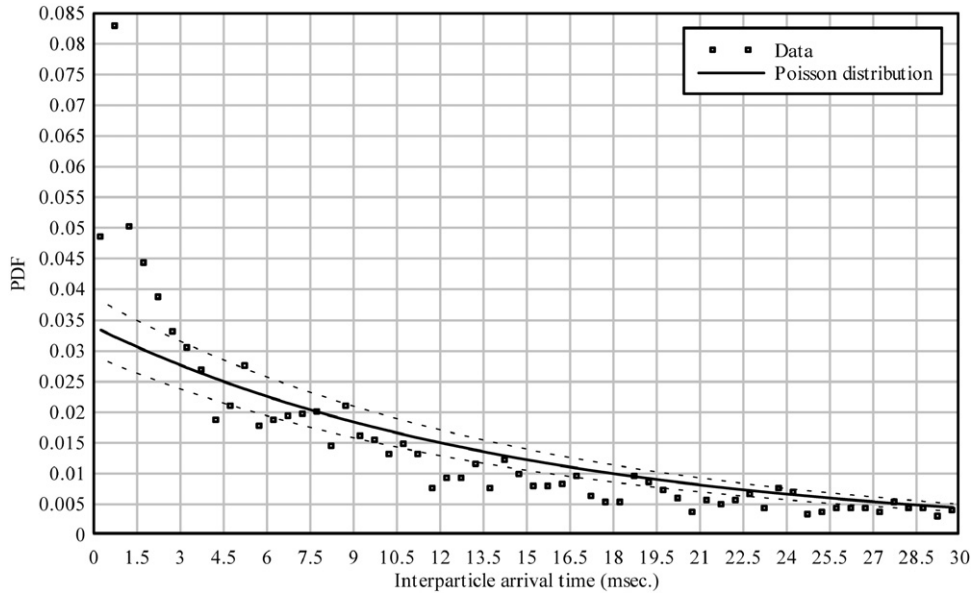
(A)
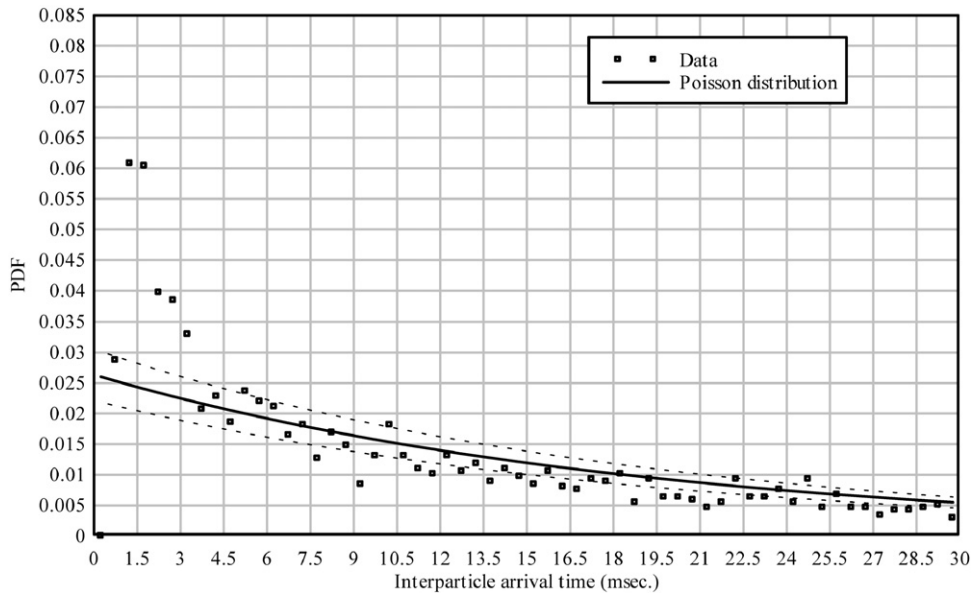
(B)

Fig. 9. Interparticle arrival time distributions in the bubbly flow region for different classes of bubble chord times with comparison between data and Poisson distribution – expected deviations from the Poisson distribution for this sample are shown in dashed lines – $Fr_1 = 8.5$, $Re_1 = 9.8\text{E}+4$, $d_1 = 0.024$ m, $x_1/d_1 = 40$, $(x - x_1)/d_1 = 12$, $W/d_1 = 20$, $y/d_1 = 1.327$, $C = 0.353$, 8000 bubbles. (A) Bubble chord times between 0 and 0.5 ms, 3055 bubbles, $\chi^2 = 461$. (B) Bubble chord times between 0.5 and 1.5 ms, 2370 bubbles, $\chi^2 = 457$. (C) Bubble chord times between 1.5 and 3 ms, 1017 bubbles, $\chi^2 = 212$. (D) Bubble chord times between 3 and 5 ms, 581 bubbles, $\chi^2 = 110$.

of bubble sizes assuming non-interacting particles. Deviations from Eq. (8) indicate some lack of randomness, or unsteadiness, and the degree of non-random particle clustering may be quantified by Chi-square tests. Practically this analysis is best conducted by breaking down the bubbly flow into narrow classes of particles of comparable sizes that are expected to have the same behaviour [20].

A simple method consists in dividing the bubble population in terms of the bubble chord time. Fig. 9 illustrates some typical interparticle arrival time distributions for four chord time classes of the same sample (0 to 0.5 ms, 0.5 to
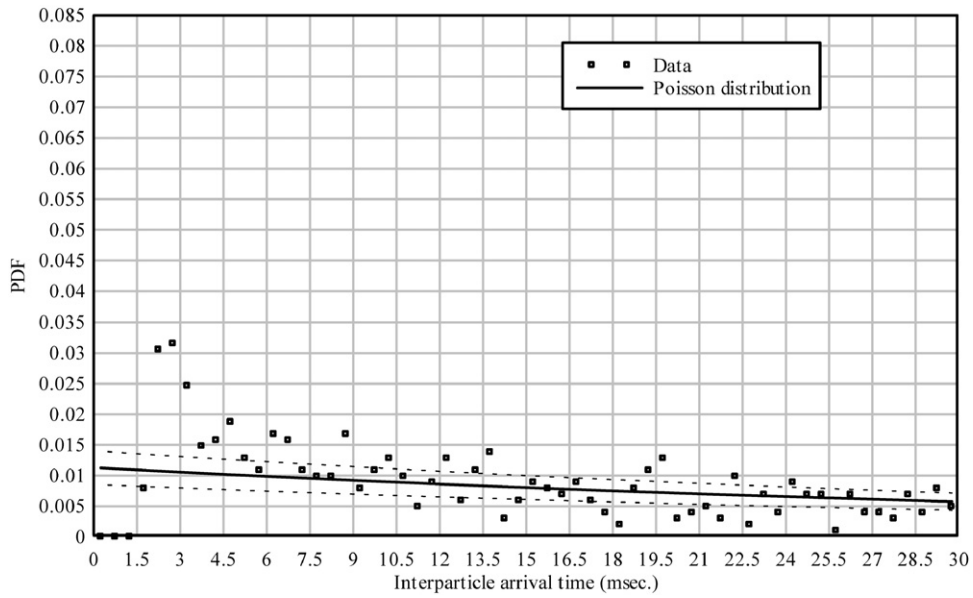
(C)
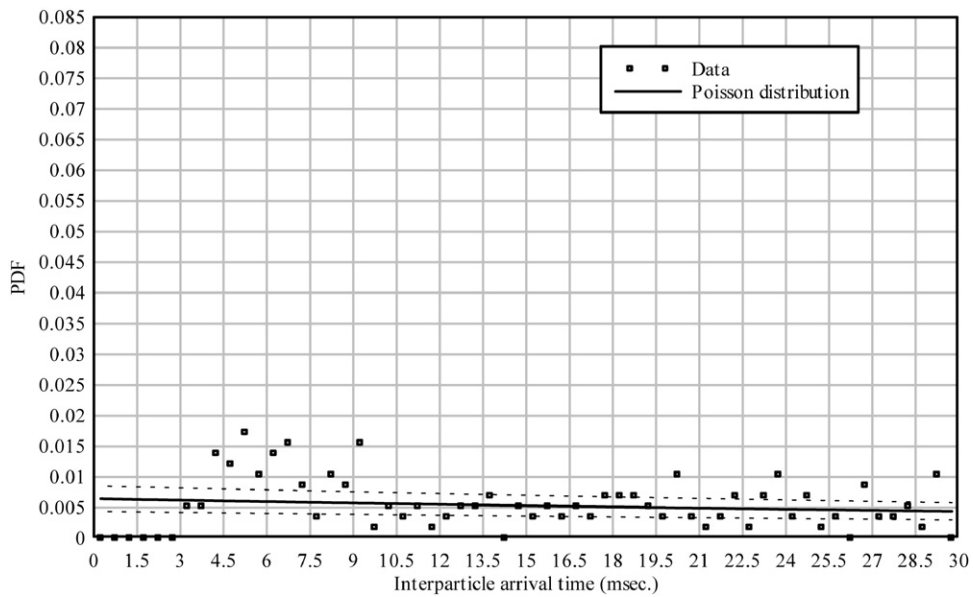
(D)

Fig. 9 (*continued*).

1.5 ms, 1.5 to 3 ms and 3 to 5 ms). The flow conditions are given in the figure caption including the Chi-square test results. For each class of bubble sizes, a comparison between data and Poisson distributions gives some information on its randomness within the assumptions underlying the derivation of the Poisson distribution. For example, Fig. 9A shows some data for bubble chord times below 0.5 ms. Clearly the smallest class of bubble chord times did not exhibit the characteristics of a random process because the experimental and theoretical distributions differ substantially in shape. For that sample, the expected deviation of a steady bubbly mixture from the theoretical curve was about $\pm 15\%$, and the second smallest interparticle time bin (0.5–1 ms) had a population that was 2.5 times the expected value or about 11 standard deviations too large (Fig. 9A). This indicates that there was a higher probability of having bubbles with shorter interparticle arrival times, hence some bubble clustering occurred.

Overall the present study showed some differences between experimental and theoretical curves. The deviations were the largest for the smallest bubble chord times (less than 3 ms) as reflected by Chi-square test results (e.g. Fig. 9). It was unlikely that the observed clustering was due to a random process.

6. Transverse time and length scales

6.1. Streamwise and transverse time scales

Correlation analyses were performed for some experiments during which two identical probes, separated by a known transverse distance z, were simultaneously scanned. Such results complement "traditional" air–water flow measurements such as void fraction and bubble count rate. Examples of vertical distributions of maximum cross-correlations $(R_{xz})_{max}$ and characteristic time scales T_{xx} and T_{xz} are presented in Fig. 10, where the time scales T_{xx} and T_{xz} are defined in Eqs. (1) and (2). Fig. 10A shows the maximum cross-correlations $(R_{xz})_{max}$ distributions for several transverse spacings z. The dimensionless void fraction distribution is also shown. Fig. 10B presents the corresponding vertical distributions of integral time scales. Note that the integral time scales are presented in dimensional forms (units: milliseconds) with a logarithmic scale (top horizontal axis).

First the results showed that the cross-correlation functions exhibited clearly a marked maximum in the advective diffusion region as illustrated in Fig. 3B. In the recirculation region and upper flow region, no clearly-defined maximum was observed and a correlation analysis could not be conducted. Second, in the advective diffusion region, the maximum cross-correlation $(R_{xz})_{max}$ was a function of the transverse spacing. Typically it decreased with an increasing transverse spacing z (Fig. 10A). Within the range of investigations (Table 2), the maximum cross-correlations dropped sharply for $z/d_1 > 0.6$. Third, the maximum cross-correlation was about independent of the inflow Froude number. Fourth, the cross-correlation time scales T_{xz} were consistently smaller than the auto-correlation time scales T_{xx}, and the former (T_{xz}) decreased with increasing transverse spacings as seen in Fig. 10B. Again the integral time scale (T_{xz}) declined rapidly for $z/d_1 > 0.6$ (Fig. 10B), and the result was consistent with lower maximum cross-correlations. Fifth the depth-averaged dimensionless time scale $T_{xx}V_1/d_1$ was about 0.8 in average. The data indicated a slight increase with increasing Froude number and longitudinal distance $(x - x_1)/d_1$ [4]. The results were best correlated by:

$$\frac{T_{xx}V_1}{d_1} = 0.019\frac{x - x_1}{d_1} + 0.1012Fr_1 - 0.1525 \tag{9}$$

with a correlation coefficient of 0.80.

The auto-correlation time scale T_{xx} is an integral time scale characterising the streamwise coherence of the two-phase flow. It represents a rough measure of the longest longitudinal connection in the air–water flow structures. On the other hand, the cross-correlation time scale T_{xz} is a time scale of transverse connection between the air–water flow structures as seen by two probes separated by a distance z. Herein, present results implied that any transverse length scale of the bubbly shear flow must be smaller than about $0.6d_1$ since negligible correlation and transverse integral time scale existed for $z/d_1 > 0.6$.

6.2. Transverse air–water length scales

For some experiments, the maximum cross-correlation coefficient $(R_{xz})_{max}$ was obtained for several transverse spacings z with identical flow conditions at identical locations. A transverse air–water length scale z was then calculated using Eq. (3). The length sale Z is a function of the inflow conditions and of the streamwise position $(x - x_1)$. Results are presented in Fig. 11. The measured void fraction distributions are also shown in Fig. 11 for completeness.

First it must be stressed that the analysis could only be performed at locations where cross-correlation calculations were meaningful. In the recirculation region and at some locations, these calculations were unsuccessful for a number of reasons that included flat cross-correlation functions without a distinctive peak, non-crossing of the correlation function(s) with the zero line, correlation functions with several peaks, meaningless correlation trends....
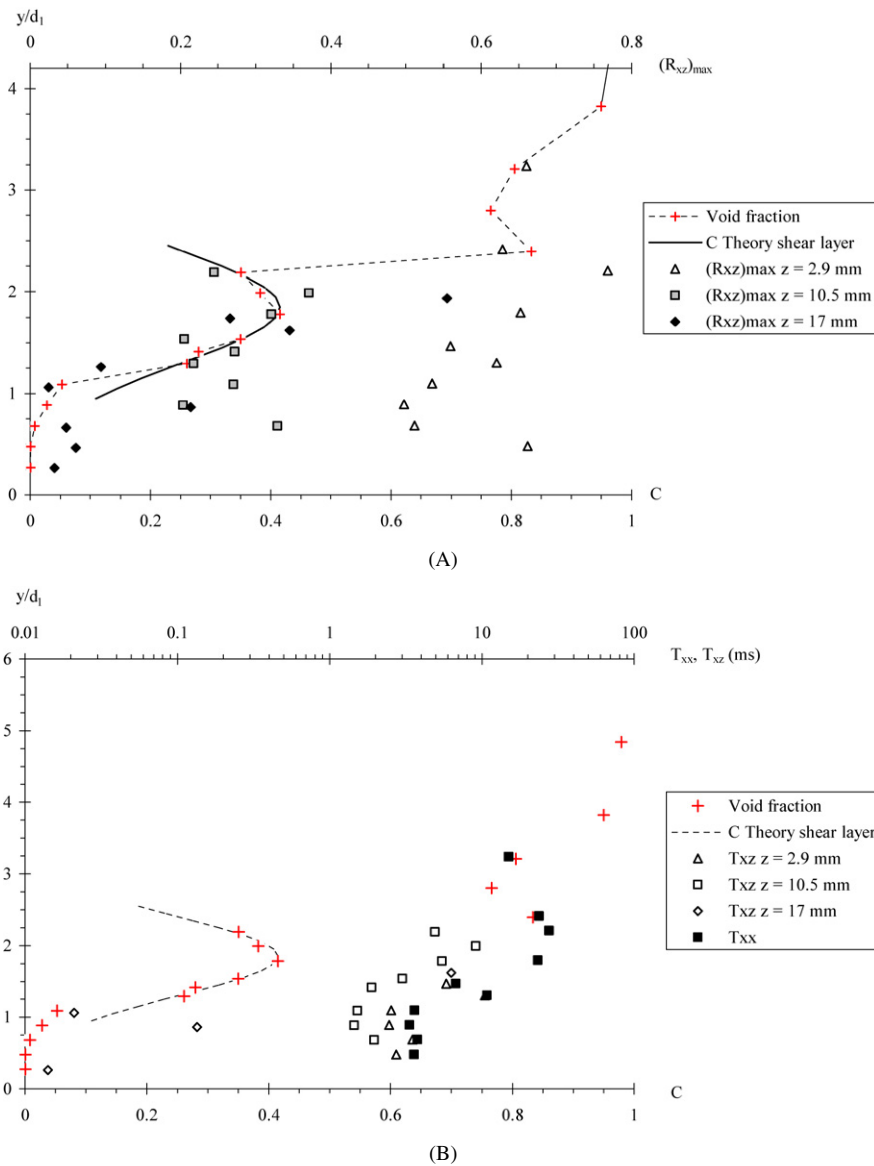
Fig. 10. Auto- and cross-correlation results in a hydraulic jump – $Fr_1 = 7.9$, $Re_1 = 9.4E+4$, $d_1 = 0.0245$ m, $x_1 = 1.0$ m, $W = 0.25$ m, $x - x_1 = 0.1$ m. (A) Vertical distributions of maximum cross-correlation $(R_{xz})_{max}$ for several transverse distances z. (B) Vertical distributions of transverse time scales T_{xx} and T_{xz} for several transverse distances.

Second the results showed that the dimensionless transverse air–water length scale Z/d_1 was about 0.25 to 0.4. The data exhibited no obvious correlation with void fraction nor bubble count rate, and they tended to show a slight increase with increasing vertical height:

$$\frac{Z}{d_1} = 0.2141 + 0.0526\frac{y}{d_1}, \qquad 0.3 < \frac{y}{d_1} < 3.3. \tag{10}$$

6.3. Discussion

Some researchers studied fundamental processes affecting free-surface deformations and air–water free-surfaces: e.g., Sarpkaya [22], Chanson [11], Brocchini and Peregrine [23], Mouaze et al. [24]. But no result on characteristic length scales in bubbly shear flows was reported and it is believed that present results are unique.
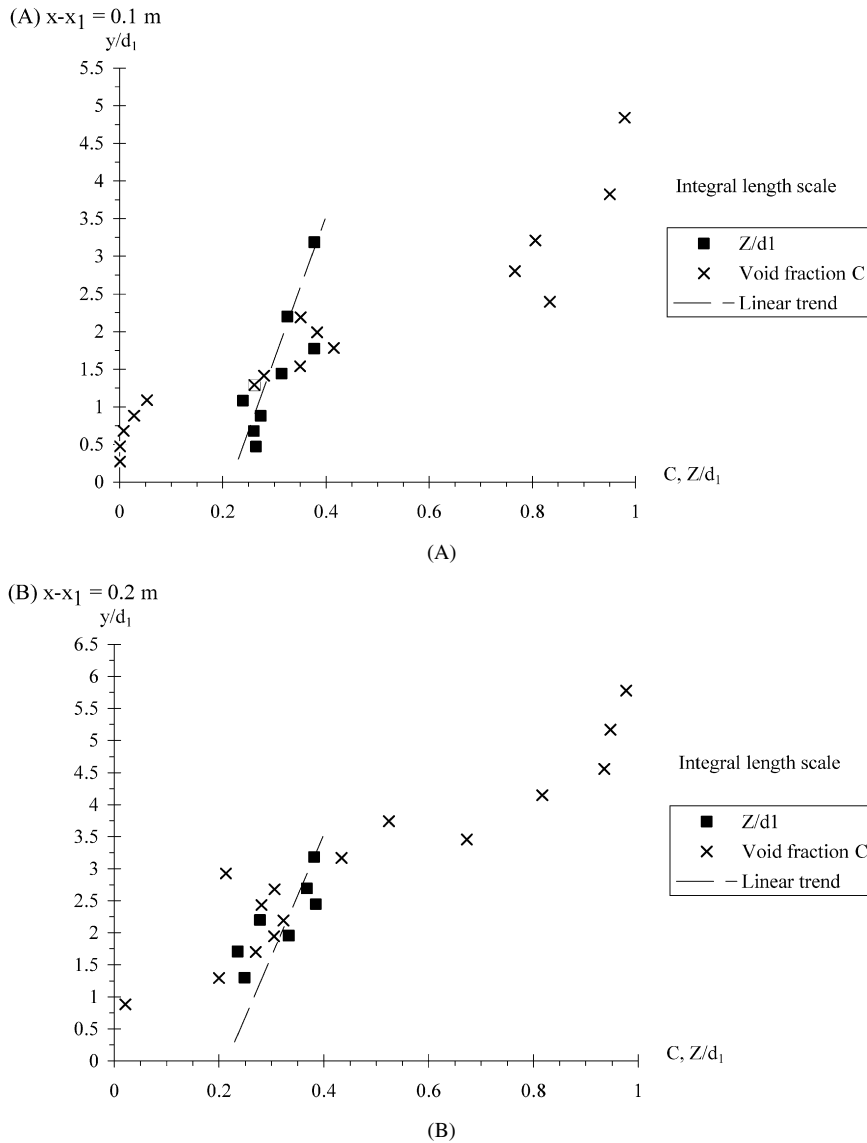
Fig. 11. Vertical distributions of dimensionless air–water transverse length scale Z/d_1 in a hydraulic jump – $Fr_1 = 7.9$, $Re_1 = 9.4E+4$, $d_1 = 0.0245$ m, $x_1 = 1.0$ m, $W = 0.25$ m – comparison with Eq. (10). (A) $x - x_1 = 0.1$ m. (B) $x - x_1 = 0.2$ m.

In the bubbly shear layer of hydraulic jumps, the characteristic length scale Z must be closely linked with the sizes of the large vortical structures and their vortex shedding. This was evidenced by high-speed photographs showing air trapping in the large eddies of the developing mixing layer (e.g. [25,11]). Basically Z is a measure of the transverse size of the vortical structures advecting air bubbles. Present results demonstrated that the transverse air–water length scales were closely related to the inflow depth: i.e., $Z/d_1 = 0.25$ to 0.4 (Fig. 11).

7. Conclusion

In an open channel, the hydraulic jump is a rapid transition from super- to sub-critical flow associated with strong turbulence and air bubble entrainment in the shear flow. New experiments were performed in some hydraulic jump flows at relatively large Reynolds numbers with two phase-detection probes. The signal analyses yielded characteristic air–water time and length scales in the mixing layer.

The void fraction measurements showed the presence of an advective diffusion shear layer in which the void fractions profiles matched closely an analytical solution of the advective diffusion equation for air bubbles. Similar results were observed in plunging jet flows and hydraulic jumps. In the developing shear region, bubble chord time distributions showed a broad range of chord times. The distributions were skewed with a preponderance of bubble chord times smaller than the mean. An analysis of the longitudinal flow structure showed comparatively little bubble clustering in the air–water shear layer region. However an interparticle arrival time analysis suggested some preferential bubble clustering for bubble chord times below 3 ms within the investigated flow conditions. Altogether both approaches are complementary, but the interparticle arrival time analyses give a greater insight into the range of particle classes affected by non-random clustering. This is believed to be a first step towards a better characterisation of air–water flow structures in turbulent shear flows.

Air–water time and length scales were integrated from auto- and cross-correlation analyses. The result provided some time and length scales of the vortical structures advecting air bubbles in the developing shear layer. The longitudinal air–water time scale was a measure of the longest longitudinal connection in the air–water flow structures and the results yielded $T_{xx}V_1/d_1 \sim 0.8$ in average. The transverse integral length scale of the eddies advecting bubbles was related to the inflow depth, and the dimensionless transverse length scale was typically about $Z/d_1 \sim 0.25$ to 0.4.

The present study showed that the hydraulic jump remains a complicated two-phase flow that is still not yet understood. The correlation and cluster analyses were a coarse preliminary approach. It is believed that more systematic applications to other turbulent shear flows may bring new insights into complex interactions between free-surface and turbulence.

Acknowledgements

References

[1] N. Rajaratnam, An experimental study of air entrainment characteristics of the hydraulic jump, J. Inst. Eng. India 42 (7) (March 1962) 247–273.

[2] B.S. Thandaveswara, Self aerated flow characteristics in developing zones and in hydraulic jumps, PhD thesis, Dept. of Civil Engrg., Indian Institute of Science, Bangalore, India, 1974, 399 p.

[3] F.J. Resch, H.J. Leutheusser, Le ressaut hydraulique: mesure de turbulence dans la région diphasique (The hydraulic jump: turbulence measurements in the two-phase flow region), J. La Houille Blanche 4 (1972) 279–293 (in French).

[4] H. Chanson, Air bubble entrainment in hydraulic jumps. Similitude and scale effects, Report No. CH57/05, Dept. of Civil Engineering, The University of Queensland, Brisbane, Australia, January 2006, 119 p.

[5] H. Chanson, Air entrainment in two-dimensional turbulent shear flows with partially developed inflow conditions, Int. J. Multiphase Flow 21 (6) (1995) 1107–1121.

[6] M. Mossa, U. Tolve, Flow visualization in bubbly two-phase hydraulic jump, J. Fluids Engrg. 120 (March 1998) 160–165.

[7] H. Chanson, T. Brattberg, Experimental study of the air–water shear flow in a hydraulic jump, Int. J. Multiphase Flow 26 (4) (2000) 583–607.

[8] F. Murzyn, D. Mouaze, J.R. Chaplin, Optical fibre probe measurements of bubbly flow in hydraulic jumps, Int. J. Multiphase Flow 31 (1) (2005) 141–154.

[9] R.A. Herringe, M.R. Davis, Detection of instantaneous phase changes in gas–liquid mixtures, J. Phys. E 7 (1974) 807–812.

[10] L. Toombes, Experimental study of air–water flow properties on low-gradient stepped cascades, PhD thesis, Dept. of Civil Engineering, The University of Queensland, 2002.

[11] H. Chanson, Air Bubble Entrainment in Free-Surface Turbulent Shear Flows, Academic Press, London, UK, 1997, 401 p.

[12] P.D. Cummings, H. Chanson, Air entrainment in the developing flow region of plunging jets. Part 1. Theoretical development, J. Fluids Engrg., Trans. ASME 119 (3) (1997) 597–602.

[13] H. Chanson, Study of air entrainment and aeration devices, J. Hydraul. Res. 27 (3) (1989) 301–319.

[14] T. Brattberg, H. Chanson, L. Toombes, Experimental investigations of free-surface aeration in the developing flow of two-dimensional water jets, J. Fluids Engrg., Trans. ASME 120 (4) (1998) 738–744.

[15] H. Chanson, S. Aoki, A. Hoque, Physical modelling and similitude of air bubble entrainment at vertical circular plunging jets, Chem. Engrg. Sci. 59 (4) (2004) 747–754.

[16] J.T.K. Luong, P.E. Sojka, Unsteadiness in effervescent sprays, Atomization & Sprays 9 (1999) 87–109.

[17] P.D. Noymer, The use of single-point measurements to characterise dynamic behaviours in spray, Experiments in Fluids 29 (2000) 228–237.

[18] H. Chanson, L. Toombes, Air–water flows down stepped chutes: turbulence and flow structure observations, Int. J. Multiphase Flow 28 (11) (2002) 1737–1761.

[19] C.F. Edwards, K.D. Marx, Multipoint statistical structure of the ideal spray, Part I: Fundamental concepts and the realization density, Atomization and Sprays 5 (1995) 435–455.

[20] C.F. Edwards, K.D. Marx, Multipoint statistical structure of the ideal spray, Part II: Evaluating steadiness using the interparticle time distribution, Atomization and Sprays 5 (1995) 435–455.

[21] J. Heinlein, U. Fritsching, Droplet clustering in sprays, Experiments in Fluids 40 (3) (2006) 464–472.

[22] T. Sarpkaya, Vorticity, free surface and surfactants, Annu. Rev. Fluid Mech. 28 (1996) 83–128.

[23] M. Brocchini, D.H. Peregrine, The dynamics of strong turbulence at free surfaces. Part 2. Free-surface boundary conditions, J. Fluid Mech. 449 (2001) 255–290.

[24] D. Mouaze, F. Murzyn, J.R. Chaplin, Free surface length scale estimation in hydraulic jumps, J. Fluids Engrg., Trans. ASME 127 (2005) 1191–1193.

[25] J.W. Hoyt, R.H.J. Sellin, Hydraulic jump as 'mixing layer', J. Hydraul. Engrg. 115 (12) (1989) 1607–1614.

[26] A.F. Babb, H.C. Aus, Measurements of air in flowing water, J. Hydraulic Division, ASCE 107 (HY12) (1981) 1615–1630.

[27] H. Chanson, S. Aoki, A. Hoque, Similitude of air bubble entrainment and dispersion in vertical circular plunging jet flows. An experimental study with freshwater, salty freshwater and seawater. Coastal/Ocean Engineering Report, No. COE02-1, Dept. of Architecture and Civil Eng., Toyohashi University of Technology, Japan, 2002, 94 p.